NANO LETTERS

pubs.acs.org/NanoLett Letter

Field-Symmetry-Engineered Magnetotransport in Magnetic NiO/Co/Pt Heterostructures

Jiafeng Feng,* Fanyu Meng, Wenbo Zhang, Haoxiang Xu, Muhammad Waqas Nafees, Ubaid Raza, Liqin Yan,* Yaowen Liu,* Yi Wang,* and Xiufeng Han

Cite This: *Nano Lett.* 2026, 26, 3258−3265 Read Online

ACCESS | Metrics & More | Article Recommendations | Supporting Information

ABSTRACT: Our study demonstrates bidirectional and reversible electrical conversion between asymmetric and symmetric magnetoresistance in NiO/Co/Pt heterostructures via magnetic field-symmetry engineering. We show that field symmetry directly dictates the emergent magnetoresistance symmetry, enabling programmable room-temperature switching among asymmetric, forward-symmetric, and reverse-symmetric configurations. This reconfigurability originates from a polarity-selective, half-field mirror inversion of resistance spikes under symmetry breaking, governed by the field-dependent reconfiguration of the rotation sequence between interfacial and bulk cobalt magnetic moments. The work establishes a novel approach to directly tailor magnetoresistance by manipulating field symmetry without altering the underlying spin transport physics, providing a prototypical platform for field-programmable spintronic devices.

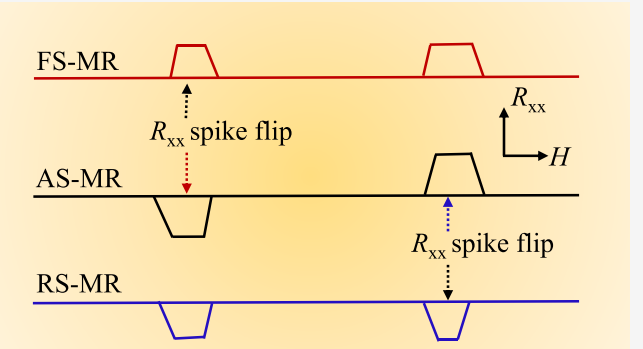

KEYWORDS: *Field symmetry, Magnetoresistance symmetry, Reconfigurable spintronics, Nonreciprocal transport*

The evolution of magnetoresistance (MR) research, from the discovery of anisotropic magnetoresistance[1] to the realization of giant magnetoresistance[2,3] and tunneling magnetoresistance,[4−6] marks a progressive deepening in the understanding of spin-dependent transport in advanced spintronics. Although these classical effects originate from distinct physical mechanisms, they generally exhibit a highly symmetric magnetic field response, with their characteristic "butterfly-shaped" magnetoresistance curves having become a paradigmatic example of symmetric control in spintronics.[5,6] In stark contrast, asymmetric magnetoresistance (AS-MR) satisfies the odd-symmetric relation $R_{xx}(H) = -R_{xx}(-H)$.[7−20] This effect originates from a magnetic-field-direction-dependent odd-symmetric transport mechanism, which breaks the field symmetry of the ferromagnetic system and is closely associated with the dynamic response of domain walls (DWs) driven by magnetization inhomogeneity. In this process, magnetic field reversal specifically breaks the time-reversal symmetry of the system, e.g., through contributions from the anomalous Hall effect (AHE). This intrinsic field asymmetry not only constitutes the defining signature of AS-MR but also represents a new dimension of advanced spin manipulation that transcends the conventional symmetry paradigm. The possibility of actively tuning field asymmetry is opening frontier pathways for nonreciprocal transport and logic operations in next-generation spin-based information devices.

Since the early 21st century, AS-MR effects have been observed in diverse material systems, including conventional metallic ferromagnets and their heterostructures (Co,[7] Co_xTb_{1-x},[8] Co/δ-Mn[9]), magnetic semiconductors ($Ga_{1-x}Mn_xAs$,[10] GaMnAs/InGaAs[11]), and two-dimensional ferromagnetic materials (Fe_3GeTe_2,[12−17] $MnPS_3/Fe_3GeTe_2$,[18] Fe_3GeTe_2/graphite/Fe_3GeTe_2[19,20]). These materials typically exhibit high tunability of magnetic domains/DWs,[7−17] providing an important platform for investigating their microscopic mechanisms and device design. While current research[7−20] has advanced the understanding of ferromagnetic behavior and the regulation of exchange coupling, a fundamental challenge remains: achieving reconfigurable magnetoresistance symmetry in AS-MR systems. Specifically, the on-demand switching among asymmetric, forward-symmetric (FS-), and reverse-symmetric (RS-) MR configurations within a single ferromagnetic material system at room temperature has not yet been achieved.

Unlike two-dimensional ferromagnetic materials, which retain their bulk magnetic properties at monolayer thickness,[21]

Received: January 9, 2026
Revised: February 13, 2026
Accepted: February 18, 2026
Published: February 23, 2026

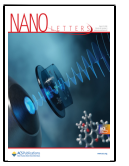

https://doi.org/10.1021/acs.nanolett.6c00125
Nano Lett. 2026, 26, 3258−3265

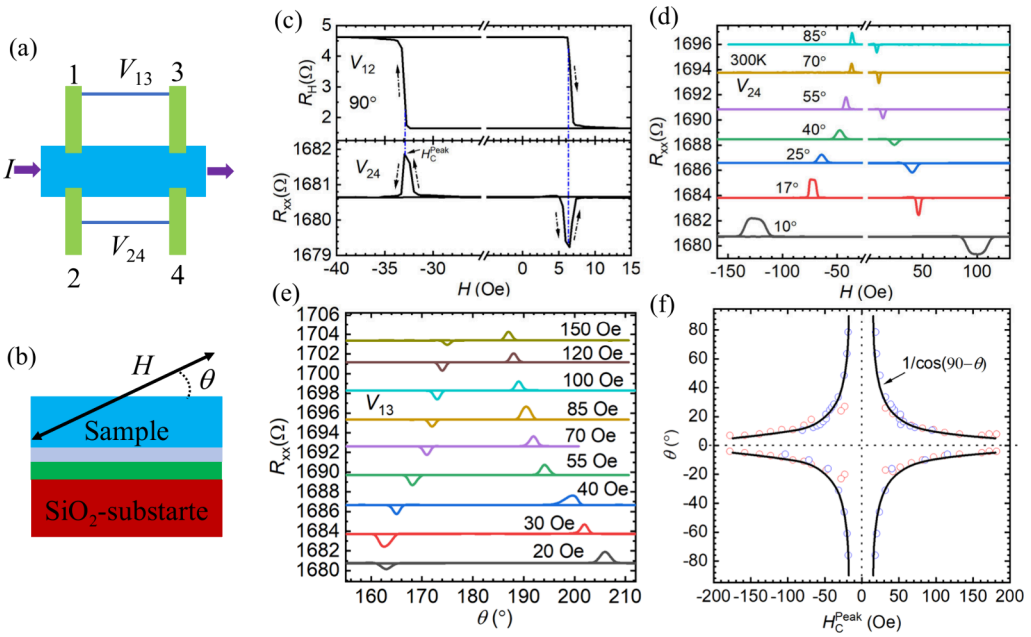

Figure 1. (a, b) Schematics of (a) Hall bar geometry and (b) angular (θ) measurement setup. Purple arrow indicates current direction; green contacts (1−4) denote voltage/current electrodes. The blue stripe represents the Hall bar in (a) and a sample cross-section is included in (b). (c) Field-dependent R_H and R_{xx} at θ = 90°. (d) Angular evolution of R_{xx}−H curves at orientations θ = 10°−85°. (e) Polar plots of R_{xx} under various positive magnetic fields. (f) Extracted θ−H_C^{Peak} relation from panels d and e and Figure S2a and b in Supporting Information S2 after removing the H_{ex} contribution from all R_{xx}−H and R_{xx}−θ curves.

conventional ferromagnets (e.g., Co) and antiferromagnets (e.g., NiO) exhibit strong thickness-dependent magnetotransport behavior.[22,23] When scaled down to atomic layers, their macroscopic magnetic properties deviate significantly from those of bulk materials,[24,25] limiting their practical use in low-dimensional spintronics. In this work, we demonstrate controlled switching between synchronous and asynchronous rotation of interfacial and bulk Co moments in ultrathin NiO/Co/Pt heterostructures. Under high magnetic fields, field-driven reorientation of NiO moments decouples the interfacial Co from the bulk Co, triggering asynchronous switching, whereas DW-mediated magnetization preserves synchronization between the two (interfacial vs bulk Co). Mechanistic analysis reveals that asynchronous rotation generates either FS-MR or RS-MR configuration, depending on which Co subsystem reverses first, as determined by the orientation of NiO moments, while synchronous rotation results in an AS-MR response. Central to this behavior is the field-tunable exchange bias in NiO/Co/Pt, which enables the simultaneous observation of all three magnetoresistance configurations—AS-MR, FS-MR, and RS-MR—in a single ferromagnetic system at room temperature. A key advancement is the demonstration of fully reversible and on-demand switching among AS-MR, FS-MR, and RS-MR configurations via controlled field symmetry manipulation. This process gates the MR symmetry between odd and even function character. The realized even symmetry, which is nonintrinsic to the ferromagnetic system, permits the MR configuration to be set into either of two opposing, arbitrarily definable orientations. This work establishes a tunable and reconfigurable multistate platform for advanced spintronic device engineering.

■ DEMONSTRATION OF AS-MR AND ITS ORIGIN

Temperature-dependent magnetometry (M−H curves, 130−300 K, see Supporting Information S1) confirms a perpendicular magnetic anisotropy in the 1.08 nm-thick Co layer for Sample S1.[26] After patterning into a four−terminal Hall−bar device (Figure 1a), magnetotransport measurements were performed on Sample S1. Field-dependent Hall resistance (R_H) and longitudinal resistance (R_{xx}) were recorded up to 10 kOe (Supporting Information S1) at different field orientations (θ, defined in Figure 1b). R_H varies linearly with the out-of-plane magnetization component, showing an antisymmetric field dependence (top panel, Figure 1c). Consistent with previous reports on $[Co/Pt]_n$ multilayers,[7] a pronounced AS-MR is observed in the R_{xx}−H curves (bottom panel, Figure 1c). The unconventional AS-MR, characterized by sharp resistance spikes, evolves markedly during magnetization reversal at the same fields where R_H changes sign. To correlate the AS-MR with the switching behavior, angular-dependent R_{xx}−H measurements were carried out. Here θ = 90° corresponds to the field applied perpendicular to the sample plane. As shown in Figure 1d, AS-MR persists at all measured angles. Notably, the magnetic field position of the resistance spike (denoted as H_C^{Peak};[14] see bottom panel of Figure 1c) shifts toward higher values as the angle θ decreases. At small angles, the spikes broaden considerably, but they gradually weaken as $\theta \rightarrow 0°$ and are eventually overwhelmed by the spin-flop signal (see Supporting Information S1).

By extracting H_C^{Peak} as a function of θ from Figure 1d and plotting the results in Figure 1f (blue symbols, quadrants I and II), we observe a nonlinear increase as θ decreases. This indicates that a smaller perpendicular field component requires a higher total field to reverse the out-of-plane magnetization (M_z) of the Co layer. As in the previous AS-MR study,[14] the θ dependence of H_C^{Peak} is well described by a 1/cos (90−θ) fit (black curve in Figure 1f), indicating that the magnetization reversal follows a Kondorsky-type model[27] where the DW motion is predominantly constrained by strain-induced pinning effects. Complementary angular-dependent AS-MR

https://doi.org/10.1021/acs.nanolett.6c00125
Nano Lett. 2026, 26, 3258−3265

data were obtained from two orthogonal measurement sets: (i) R_{xx} (H) curves taken while sweeping from 90° to 180° (see Supporting Information S2), and (ii) R_{xx} (θ) curves measured under fixed positive and negative fields (Figure 2e and Figure S2b in Supporting Information S2). The extracted H_C^{Peak} values (after subtracting the exchange-bias field, H_{ex}) are plotted as blue and red symbols in Figure 1f, respectively. Although continuous angular coverage between −50° and +50° was experimentally inaccessible, measurements over 130°−220° provided a consistent data set (Supporting Information S3). The two independent methods yield fully consistent $H_C^{Peak}(\theta)$ dependencies, together establishing a perfectly symmetric angular variation. These systematic $H_C^{Peak}(\theta)$ results—like those seen in current-driven DW depinning[28]—provide strong evidence for the formation, stabilization, and annihilation of circulating currents near the DWs, which we identify as the key origin of the AS-MR in our system. The fitted 1/cos (90−θ) curves (black lines in Figure 1f) mark the peak intensity of such circulating currents.

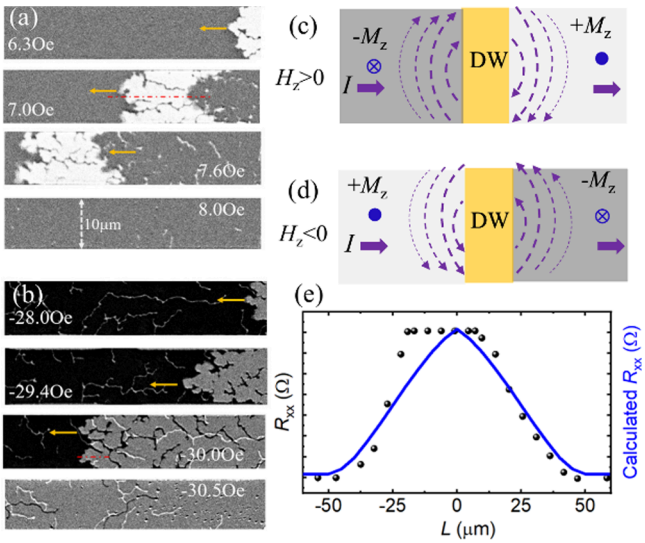

Figure 2. (a, b) MOKE images under perpendicular fields (H_z) of opposite polarity. White, gray, and dark regions denote different out-of-plane magnetizations M_z. Yellow arrows indicate DW propagation direction. (c, d) Schematic distributions of localized circulating currents around DWs for $H_z > 0$ and $H_z < 0$. Purple arrows show the d.c. current direction; dashed purple curves illustrate the exponential decay of current intensity with distance from the DW core. (e) Measured R_{xx} (black dots) as a function of DW position, compared with the theoretical curve (blue line) from eq 1.

In AS-MR research, magneto−optical Kerr effect (MOKE) microscopy[7−9,11,13,16] and magnetic force microscopy[17] have been widely used to track the dynamics of magnetic domains and their DWs directly. These studies consistently reveal a direct link between domain configurations and AS-MR,[7] a correlation confirmed by our own MOKE observations (Figure 2). After saturating the sample in a large negative field, a small positive field was applied and gradually increased. A bubble-like +M_z domain (white) initially appears at one end of the Hall bar (Figure 2a) and propagates as the field rises, while the surrounding −M_z region (gray) forms a DW with 180° magnetization reversal across it (Figure 2c). Conversely, after positive saturation, a negative field first induces −M_z (gray) domains at the bar end, which then expand until the original +M_z (dark) domains are fully replaced (Figure 2b), with a sharp DW maintained between opposite domains throughout (Figure 2d). MOKE thus allows us to visualize not only the reproducible field-driven evolution of domains and DWs, but also the progressive propagation of DWs along the Hall bar, providing direct insight into DW dynamics during transport. As the DW moves across the electrode spacing L with increasing field, the measured R_{xx} exhibits three distinct stages: a gradual rise, a plateau, and a decay (Figure 2e), corresponding to the positive/negative resistance spikes at H_C^{Peak} in the R_{xx}−H curves.[7] The following equation well captures this behavior:[13]

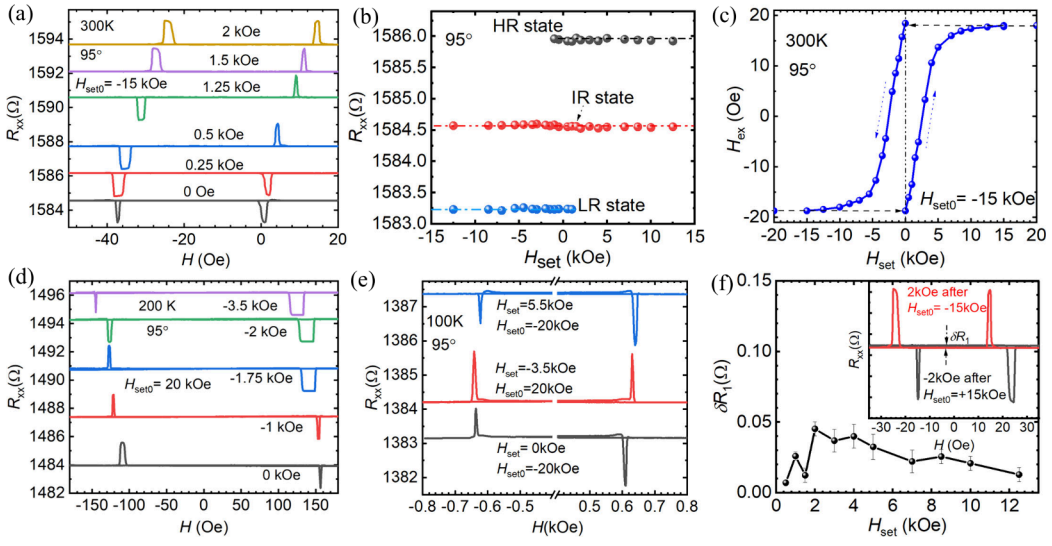

Figure 3. (a) R_{xx}−H curves measured at 300 K and θ = 95° under different H_{set} fields, starting from a preset H_{set0} = −15 kOe. (b) Dependence of the HR, IR, and LR states on H_{set}. (c) Dependence of H_{ex} on H_{set} at 300 K and θ = 95°, extracted from R_{xx}−H curves in Figure 3a (H_{ex} at H_{set0} = −20 kOe from Figure S4 in Supporting Information S4). (d) R_{xx}−H curves at 200 K and θ = 95° for varying H_{set}, with H_{set0} = 20 kOe. (e) R_{xx}−H curves at 100 K and θ = 95° for different H_{set}, initially set with H_{set0} = ± 20 kOe. (f) Difference δR_1 in R_{xx} between curves measured with opposite but equal-magnitude H_{set}, plotted as a function of H_{set}. The inset in (f) shows a case of δR_1 at H_{set} = ±2 kOe.

https://doi.org/10.1021/acs.nanolett.6c00125
Nano Lett. 2026, 26, 3258−3265

$$R_{xx} = \frac{\rho L}{wt} + R_H\left[\frac{4}{\pi^2}\sum -\theta_H\left(\frac{L}{2} - |x_{DW}|\right)\right]$$

$$\sum = \sum_{n=old} \frac{\exp\left(-\frac{\pi n}{a}\left|\left(x_{SE} + \frac{L}{2}\right)\right|\right) - \mathrm{sgn}\left(|x_{SE}| - \frac{L}{2}\right)\exp\left(-\frac{\pi n}{a}\left|\frac{L}{2}\right| - x_{SE}\right)}{n^2} \quad (1)$$

where t and w are the sample thickness and width, θ_H is the Hall angle, x_{DW} is the DW position, and x_{SE} is the step−edge coordinate along the width (applicable with or without a physical terrace). A good agreement between eq 1 (Figure 2e, blue curve) and the experimental data confirms that the AS-MR originates from AHE-driven circulating currents localized near the DW.[7,13] Mapping the domain and DW distributions under opposite H_z polarities ($H_z > 0$ in Figure 2c and $H_z < 0$ in Figure 2d, where H_z is applied at $\theta \approx 90°$) shows that a small d.c. current induces circulating currents around the DW (the purple dashed lines in Figure 2c, d). These currents, which decay away from the DW core, skew electron trajectories and produce opposite voltage polarities in $+M_z$ and $-M_z$ domains. For $H_z > 0$ (Figure 2c), a clockwise circulation gives $V_{13} > 0$ and $V_{24} < 0$; reversing H_z (Figure 2d) yields a counterclockwise circulation and inverted voltages ($V_{13} < 0$, $V_{24} > 0$). The results directly demonstrate how AHE-driven circulating currents couple to the local magnetization and how the field polarity controls their sense.

FIELD-SYMMETRY CONTROLLED AS-MR TO FS-MR OR RS-MR

To systematically study the active engineering of MR symmetry through field-symmetry control, we developed a two-step magnetic field protocol. The procedure begins with initializing the system at a high perpendicular preset field (H_{set0}), followed by applying a reverse field (H_{set}) before performing $R_{xx}-H$ measurements under small probing fields ($|H| < |H_{set}|$). This protocol, illustrated in Figure 3a for $H_{set0} = -15$ kOe ($\theta = 95°$) and $H_{set} \geq 0$, enables continuous and reversible switching among all three MR configurations—AS-MR, FS-MR, and RS-MR. Among them, the AS-MR configuration exhibits three resistance states, including high-resistance (HR) state, low-resistance (LR) state, and intermediate-resistance (IR) state. FS-MR exhibits an IR state along with a HR state, shown by two R_{xx} spikes above the IR level in both positive and negative magnetic fields. Conversely, RS-MR shows an IR state accompanied by a LR state, revealed through two R_{xx} spikes below the IR level, symmetrically located across the magnetic field range. As illustrated in Figure 3b, the corresponding HR, IR and LR states extracted from Figure 3a exhibit good stability as a function of the H_{set} field. Furthermore, the interconversion among AS-MR, FS-MR and RS-MR is controlled by both the magnitude and polarity of H_{ex}, which is tuned via H_{set0} and H_{set} (Figure 3c). By mapping the critical H_{ex} ranges corresponding to each type of MR configuration, we achieve deterministic switching between any two types of MR configurations through precise control of H_{ex}. Temperature-dependent measurements confirm reproducibility: at 300 K, $R_{xx}-H$ curves are fully reproducible after $H_{set0} \geq 10$ kOe (Figure 3c), while at lower temperatures (200 K in Figure 3d, 100 K in Figure 3e), enhanced H_{ex} due to stronger interfacial coupling suppresses FS-MR at $H_{set} = 0$ and stabilizes AS-MR under small H_{set}, yet all MR interconversions remain functional. To summarize, while AS-MR, FS-MR, and RS-MR are all regulated by H_{ex} via H_{set0} and H_{set} (Figure 3), the transition between these MR configurations is achieved by manipulating magnetic field symmetry. This conversion represents a nonreciprocal magnetotransport response originating from field-symmetry breaking, exhibiting polarity-selective behavior that establishes half-field mirror symmetry in the magnetoresistance, as will be elaborated upon in the following section.

EXPLANATION OF FIELD-SYMMETRY CONTROLLED AS-MR TO FS-MR OR RS-MR

Unlike AS-MR, both FS-MR and RS-MR exhibit even symmetry. Specifically, FS-MR follows the relation $+R_{xx}(H) = +R_{xx}(-H)$, which corresponds to upward resistance spikes of identical polarity in both magnetic field directions. This behavior indicates the presence of two HR states across positive and negative field ranges, often described as a positive MR configuration. Conversely, RS-MR obeys $-R_{xx}(H) = -R_{xx}(-H)$, resulting in downward resistance spikes of opposite polarity during the two field sweeps. This reflects the formation of two LR states over the positive and negative field ranges, commonly referred to as a negative MR configuration. Building on this, the transition mechanism from AS-MR to FS-MR or RS-MR can be described as an inversion of asymmetric R_{xx} between positive and negative magnetic fields under field-symmetry breaking. Specifically, resistance spike in one polarity undergoes mirror inversion—for instance, downward spike flips to upward—while the spike morphology remains unchanged in the opposite polarity. This process yields a symmetric profile (Figure 3) and provides a clear physical representation of how field-symmetry breaking influences magnetoresistance symmetry. In Sample S1 under large H_{set0} and H_{set} fields, asynchronous magnetization rotation (more see Supporting Information S5) occurs between the bulk Co layer (adjacent to Pt) and the interfacial Co layer (adjacent to NiO).[29] This behavior is facilitated by the 1.31 nm NiO, which loses antiferromagnetic order near room temperature and hosts rotatable magnetic moments—a conclusion supported by electron spin resonance (ESR) measurements (Figure S6 in Supporting Information S6). The ESR spectra distinctly show two separate magnetic signals, corresponding precisely to the interfacial and bulk Co layers. H_{ex} modulation stems from reorganization of NiO moments at the NiO/Co interface, influencing moment rotation in two Co layers (Figure 3) due to the superparamagnetic behavior of interfacial cobalt that enables its magnetic moments to decouple from those of the bulk Co layer (Figure S6 in Supporting Information S6). Under large $H_{set0} = \pm 10$ kOe, distinct rotation dynamics are observed (Figure 4a) when the interfacial Co is primarily influenced by NiO and couples tightly with it. The asynchronous, sequential rotation of the two Co layers drives the R_{xx} inversion and MR transition from AS-MR to either FS−MR or RS−MR. For $H_{set0} = +10$ kOe, bulk Co rotates first in positive fields and interfacial Co first in negative fields; this inverts for $H_{set0} = -10$ kOe. The rotation order dictates H_C^{Peak} position: it appears after bulk Co rotation if bulk Co rotates first, and before if interfacial Co rotates first. Asynchronous rotation occurs under: (i) large H_{set0} with $H_{set} \approx 0$ (Figure S4 in Supporting Information S4, Figure 4a), and (ii) large H_{set} that substantially alters H_{ex} (Figure 3a). Synchronous rotation prevails at intermediate $\pm H_{set}$, where only bulk Co rotates in both field polarities due to a uniform bulk-like Co layer (Figure 3a, Figure 4b). The above conclusion is further

https://doi.org/10.1021/acs.nanolett.6c00125
Nano Lett. 2026, 26, 3258−3265

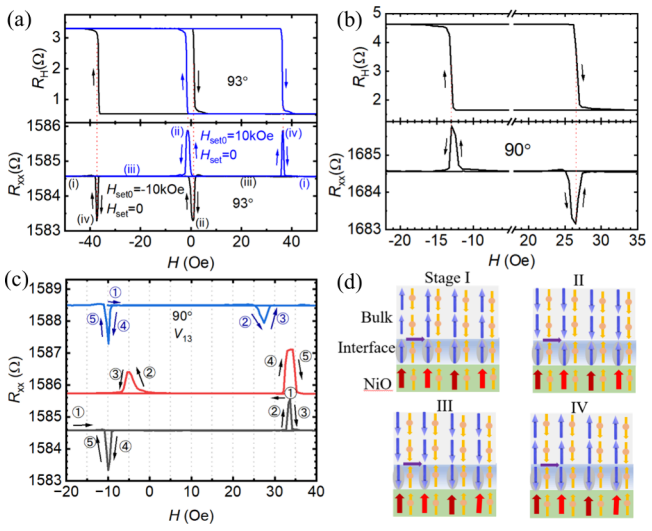

Figure 4. (a) R_H–H and R_{xx}–H curves measured at 300 K, θ = 93° with initial fields H_{set0} = ±10 kOe (H_{set} = 0). (b) R_H–H and R_{xx}–H characteristics at 300 K, θ = 90°. (c) R_{xx} − H curves measured starting from the field around the completion of bulk Co rotation on one magnetic field side, scanning toward the opposite field direction where the interfacial Co moments begin to respond. Labels ①–⑤ denote the order of magnetic field scanning. (d) Schematic of spin polarization and magnetization in interfacial and bulk Co under positive H_{ex}. The schematic shows that the interfacial cobalt layer's region of influence includes the neighboring nickel oxide monolayer. This result is obtained under the condition of an identical spin current in both. Four resistance states are identified: IR (stages I and III), LR (stage II), and HR (stage IV). Blue and brown/red arrows indicate magnetization in Co and NiO layers, respectively; purple arrows show charge current; yellow arrows with spheres denote spin polarization from spin–momentum locking.

corroborated by MOKE imaging results (Figure S7 in Supporting Information S7). We find that AS-MR is associated with a fragmented multidomain state, while symmetric MR (FS-MR or RS-MR) corresponds to a uniform single-domain configuration, as the system evolves from a domain wall-scattering-dominated regime to a coherent single-domain structure.

In the R_{xx}–H curves, the width of resistance spikes exhibits clear polarity asymmetry when interfacial Co moments rotate first, whereas no such asymmetry is observed when bulk Co moments rotate across both field polarities (Figures 1c, 4b).[7−17,19,20] Supplementary validations with in-plane (IP) H_{set0} at 300 K and θ = 90° show enhanced asynchronization between interfacial and bulk Co layers under large IP H_{set0}, along with distinct R_{xx}–H and R_H–H plateaus at different H_{set} (see Figure S8 in Supporting Information S8). Moreover, R_{xx}–H curves measured starting from the field around the completion of bulk Co rotation (Figure 4c), scanning toward the opposite field direction where the interfacial Co moments begin to respond due to its superparamagnetism. In this configuration, the resistance spike in the opposite field polarity undergoes mirror inversion relative to the intermediate-resistance baseline, transforming the response from AS-MR to either FS-MR or RS-MR (Figure 4c). This demonstrates a transition in the magnetoresistance symmetry from odd to even, defined by the change from $R_{xx}(+H) = -R_{xx}(-H)$ to $R_{xx}(+H) = R_{xx}(-H)$ or $-R_{xx}(+H) = -R_{xx}(-H)$, confirming that broken field symmetry drives such symmetry transitions—a process governed by the field-dependent reordering of rotation between interfacial and bulk magnetic moments, which similarly regulates both forward and reverse conversions between asymmetric and symmetric magnetoresistance configurations. The lower coercivity of the interfacial Co layer compared to the bulk Co further corroborates the presence of a distinct interfacial phase (Figure 4c). It is noteworthy that the formation of such an interfacial phase is subject to rather stringent conditions. In a newly grown control sample (Sample S3) deliberately fabricated without an interfacial Co layer, the characteristic response illustrated in Figure 3 is absent (see Figure S9 in Supporting Information S9). Moreover, for Sample S2, which was grown concurrently but incorporated a thicker NiO layer, an interfacial Co layer did form; however, the pronounced interfacial pinning exerted by the thick NiO suppresses the emergence of the response seen in Figure 3, and this feature is likewise missing (see Figure S10 in Supporting Information S10). Similarly, when the NiO layer is omitted in Sample S4, the response depicted in Figure 3 is also absent (see Figure S11 in Supporting Information S11). This clear difference provides direct evidence that the transformation of the magnetoresistance response from AS-MR to either FS-MR or RS-MR is a distinct effect arising exclusively in structures possessing both interfacial and bulk Co layers with oppositely oriented spin currents (as shown below).

The transition from asymmetric to symmetric MR is driven by field-symmetry changes via the rotation sequence of interfacial and bulk Co moments, with field symmetry determining whether MR is forward-symmetric, reverse-symmetric, or asymmetric, while the underlying spin-dependent transport physics is preserved. This mechanism explains the observed asymmetric R_{xx} between field polarities under symmetry breaking, where resistance spikes invert in one polarity but remain unchanged in the opposite. In the following, we provide a detailed explanation of this asymmetric R_{xx} behavior under field-symmetry breaking. In our magnetic heterostructure, a d.c. current through the Co/Pt layers generates a spin current with opposite spin orientations in the interfacial and bulk Co regions via spin–orbit coupling.[18] Under H_{set0} = ±10 kOe (H_{set} = 0), δR_1 approaches zero (Figure 3f), a behavior resulting from the coupling between rotatable NiO moments[30,31] and the interfacial Co layer. Spin-current reflection at the NiO/Co interface generates an interfacial spin current oriented opposite to that in the bulk Co. Under these conditions, the enhanced magnetic moment of the interfacial Co causes the amplitude of the reflected spin current to become comparable to that of the bulk Co, leading to their effective cancellation and consequently the near-zero δR_1 at H_{set0} = ±10 kOe or a reduced δR_1 under large H_{set} (Figure 3f). It is noteworthy that δR_1 originates from the difference in the IR state (the inset of Figure 3f) between the two R_{xx}–H curves measured at ±H_{set}, primarily due to the opposite orientations of NiO moments under the same spin-current direction. When a magnetic field is applied, spin polarization aligns either parallel or antiparallel to the magnetization in two Co regions (Figure 4d).[29] The antiparallel configuration causes stronger electron scattering than the parallel case, resulting in high-resistance and low-resistance states,[18] respectively.

The analysis of Figure 4d reveals that engineering magnetoresistance symmetry via field-symmetry control rests entirely on a material platform that manifests AS-MR. The resistance evolution can thus be categorized into four distinct stages (Figure 4d) in our case: stages I and III correspond to the IR

https://doi.org/10.1021/acs.nanolett.6c00125
Nano Lett. 2026, 26, 3258−3265

state, stage II to the LR state, and stage IV to the HR state. Additional details regarding these stages and their corresponding spin configurations are provided in Supporting Information S12. For H_{set0} = +10 kOe and H_{set} = 0, starting with bulk Co aligned along $+M_z$, a positive-to-negative sweep proceeds as (i) stage I (IR), (ii) interfacial Co rotates → stage IV (HR)—the resistance spike undergoes mirror inversion within the negative magnetic field range in the R_{xx}−H curve, (iii) bulk Co reverses → stage III (IR), and (iv) on the return sweep, bulk Co rotates first to stage IV (HR) before interfacial Co realigns to stage I. This yields FS−MR (see Figure S12a in Supporting Information S13). For H_{set0} = −10 kOe and H_{set} = 0, the reversed initial alignment produces LR states across both polarities and analogous step−wise analysis confirms the presence of RS−MR—the resistance spike undergoes mirror inversion within the positive magnetic field range in the R_{xx}−H curve (see Figure S12b in Supporting Information S13). Thus, the transition from AS-MR to either FS-MR or RS-MR is governed by the field-polarity-dependent rotation sequence of the interfacial and bulk Co moments, which directly dictates the mirror inversion of the resistance spike within a specific field range in the R_{xx}−H curve due to the magnetic field breaking. While the fundamental resistance states (HR, LR, IR) are determined by spin-dependent scattering, the resulting symmetry of the magnetoresistance—whether forward-symmetric, reverse-symmetric, or asymmetric—is controlled through field-driven reordering of the moment rotation sequence. This model provides a coherent explanation of how field symmetry influences MR symmetry within the framework of spin-dependent transport in advanced spintronics. A crucial point to note is that the distinction between FS-MR and RS-MR arises from considering the rotatable magnetic moment of NiO and the presence of positive/negative H_{ex}. As evidenced by the comparison in Figure S12a, b (Supporting Information S13), it is precisely these two factors that lead to the diametrically opposed outcomes of FS-MR and RS-MR.

In the study of magnetoresistance,[32−40] precisely classifying the symmetry of response functions is a central task. Although both FS-MR and RS-MR obey an even-symmetry relation, their mathematical expressions are different (see above). The ability to accurately realize and distinguish between FS-MR and RS-MR constitutes a crucial step toward the precision engineering of magnetoresistance response function symmetries. More importantly, the identification and reversible control of these two inherently distinct even-symmetric configurations are of fundamental significance for constructing novel spintronic devices based on symmetry engineering,[32−35] as they provide a richer physical framework for realizing multistate information storage and robust sensing functionalities. Our work directly addresses this critical issue. For the first time, we demonstrate not only a fully reversible transition between FS-MR and RS-MR, but also a transition from AS-MR to either symmetric form, achieved using only a single ferromagnetic material and tunable preset magnetic fields (H_{set0}/H_{set}). This transition is accompanied by clearly distinguishable, polarity-specific inversions of resistance spikes, which can be directly observed in experiments. Our findings establish a generalizable strategy for MR symmetry engineering that goes beyond static material design. By integrating precise symmetry classification, reversible interconversion, and theoretical elucidation, we expand the functional space of advanced spintronic devices toward high-density, reconfigurable architectures.[41] This marks a paradigm shift in the field of magnetoresistance toward programmability through dynamic symmetry control.

In summary, we have demonstrated dynamic and reversible control of magnetoresistance symmetry in NiO/Co/Pt heterostructures at room temperature. This is achieved by programming field symmetry to switch between synchronous and asynchronous rotation of interfacial and bulk Co moments, which in turn enables controlled switching from AS-MR to either FS-MR or RS-MR, achieving deterministic interconversion among the three distinct magnetoresistance configurations. Crucially, these transitions are governed by a common magnetotransport mechanism stemming from field-symmetry breaking: polarity-selective inversion of the resistance spike under specific field orientations establishes half-field mirror symmetry, while the underlying spin-dependent transport physics remains intact. By establishing field symmetry as a direct and programmable handle for tailoring magnetoresistance, this work provides a versatile multistate platform and a generalizable design paradigm for adaptive spintronic devices, including reconfigurable logic and field-responsive memory systems.

METHODS

Sample Preparation

The samples were fabricated on a Si/SiO_2 substrate using a ULVAC TMR R&D magnetron sputtering system (MPS-4000-C6) with a base pressure of 2×10^{-6} Pa. The investigated samples were fabricated in two distinct batches and categorized into a primary sample and a series of comparators. The primary sample, S1, and comparator S2 (both grown in September 2017) feature NiO (1.15 and 2.31 nm, respectively)/Co (1.08 nm)/Pt (3 nm). To further elucidate the role of the NiO capping layer in a more recent fabrication batch, we prepared an additional series of comparator samples (S3 and S4, grown in November 2024): Sample S3 comprises NiO (2 nm)/Co (0.8 nm)/Pt (3 nm), while Sample S4, a critical control, lacks the NiO layer entirely, consisting of Pt (1 nm)/Co (0.8 nm)/Pt (3 nm). The Co and Pt layers were deposited via DC sputtering, while NiO was deposited via AC sputtering; no in-plane magnetic field was applied during growth. To ensure high-quality interfaces, a sufficiently low deposition rate was employed, with, for example, over 7 s required to deposit a single monolayer of Co.[42] Following deposition, all samples were annealed at 300 °C for 1 h under a 0.8 T out-of-plane magnetic field to enhance perpendicular magnetic anisotropy.

Device Fabrication and Characterization

Electrical contacts were patterned into a Hall bar geometry (Figure 1a) using UV lithography, followed by Ar^+ ion milling and lift-off. A bilayer of Pt (5 nm)/Au (80 nm) was then deposited by magnetron sputtering to form the contact electrodes, resulting in Hall bars with dimensions of 10 μm (width) × 100 μm (length). Magnetic and magnetotransport measurements were performed using a Physical Property Measurement System (PPMS, Quantum Design). Measurements were conducted in a temperature range of 100−300 K and a magnetic field range of ±30 kOe. A constant d.c. current of 0.1 mA was applied for magnetotransport measurements.

ASSOCIATED CONTENT

Supporting Information

The Supporting Information is available free of charge at https://pubs.acs.org/doi/10.1021/acs.nanolett.6c00125.

Magnetic and magnetotransport properties for Samples S1−S4; resistance state evolution for FS-MR and NS-MR configuration (PDF)

https://doi.org/10.1021/acs.nanolett.6c00125
Nano Lett. 2026, 26, 3258−3265

AUTHOR INFORMATION

Corresponding Authors

Jiafeng Feng − *Beijing National Laboratory for Condensed Matter Physics, Institute of Physics, Chinese Academy of Sciences, Beijing 100190, China; School of Physical Sciences, University of Chinese Academy of Sciences, Beijing 100049, China;* orcid.org/0000-0003-3035-8145; Email: jiafengfeng@iphy.ac.cn

Liqin Yan − *Beijing National Laboratory for Condensed Matter Physics, Institute of Physics, Chinese Academy of Sciences, Beijing 100190, China*; Email: lqyan@iphy.ac.cn

Yaowen Liu − *School of Physical Science and Engineering, Tongji University, Shanghai 200082, China;* orcid.org/0000-0001-8591-4466; Email: yaowen@tongji.edu.cn

Yi Wang − *Key Laboratory of Materials Modification by Laser, Ion and Electron Beams (Ministry of Education), School of Physics, Dalian University of Technology, Dalian 116024, China;* orcid.org/0000-0002-1747-0899; Email: yiwang@dlut.edu.cn

Authors

Fanyu Meng − *Key Laboratory of Materials Modification by Laser, Ion and Electron Beams (Ministry of Education), School of Physics, Dalian University of Technology, Dalian 116024, China*

Wenbo Zhang − *School of Physical Science and Engineering, Tongji University, Shanghai 200082, China*

Haoxiang Xu − *School of Physical Science and Engineering, Tongji University, Shanghai 200082, China*

Muhammad Waqas Nafees − *Beijing National Laboratory for Condensed Matter Physics, Institute of Physics, Chinese Academy of Sciences, Beijing 100190, China*

Ubaid Raza − *Beijing National Laboratory for Condensed Matter Physics, Institute of Physics, Chinese Academy of Sciences, Beijing 100190, China;* orcid.org/0009-0004-4768-0055

Xiufeng Han − *Beijing National Laboratory for Condensed Matter Physics, Institute of Physics, Chinese Academy of Sciences, Beijing 100190, China*

Complete contact information is available at: https://pubs.acs.org/10.1021/acs.nanolett.6c00125

Notes

The authors declare no competing financial interest.

ACKNOWLEDGMENTS

This work was financially supported by the National Key Research and Development Program of China (MOST Grant No. 2022YFA140280), the National Natural Science Foundation of China (NSFC, Grant Nos. T2495210, T2495211, 12134017, 12174425, 12274322, 52471254, 12261131506, and 12074052), the Natural Science Foundation of Liaoning Province of China (2021-YQ-06), and the Fundamental Research Funds for the Central Universities (DUT24GJ204).

REFERENCES

(1) Thomson, W. On the electro−dynamic qualities of metals: − effects of magnetization on the electric conductivity of Nickel and of ion. *Proc. R. Soc. London, Ser. A* **1857**, No. 8, 546−550.

(2) Baibich, M. N.; Broto, J. M.; Fert, A.; Van Dau, F. N.; Petroff, F.; Etienne, P.; Creuzet, G.; Friederich, A.; Chazelas, J. Giant magnetoresistance of (001)Fe/(001)Cr magnetic superlattices. *Phys. Rev. Lett.* **1988**, *61*, 2472−2475.

(3) Binasch, G.; Grünberg, P.; Saurenbach, F.; Zinn, W. Enhanced magnetoresistance in layered magnetic structures with antiferromagnetic interlayer exchange. *Phys. Rev. B* **1989**, *39*, 4828−4830.

(4) Julliére, M. Tunneling between ferromagnetic films. *Phys. Lett. A* **1975**, *54*, 225−226.

(5) Miyazaki, T.; Tezuka, N. Giant magnetic tunneling effect in Fe/Al_2O_3/Fe junction. *J. Mag. Mag. Mater.* **1995**, *139*, L231−L234.

(6) Moodera, J. S.; Kinder, L. R.; Wong, T. M.; Meservey, R. Large Magnetoresistance at room temperature in ferromagnetic thin film tunnel junctions. *Phys. Rev. Lett.* **1995**, *74*, 3273−3726.

(7) Cheng, X. M.; Urazhdin, S.; Tchernyshyov, O.; Chien, C. L.; Nikitenko, V. I.; Shapiro, A. J.; Shull, R. D. Antisymmetric magnetoresistance in magnetic multilayers with perpendicular anisotropy. *Phys. Rev. Lett.* **2005**, *94*, No. 017203.

(8) Su, Y. T.; Meng, Y.; Shi, H. B.; Wang, L.; Cao, X. Y.; Zhang, Y.; Li, R. W.; Zhao, H. W. Antisymmetric magnetoresistance due to domain-wall tilting in perpendicularly magnetized films. *Phys. Rev. Appl.* **2022**, *17*, No. 014013.

(9) Han, R. K.; Liu, L.; Sun, H. L.; Qin, H. R.; Zhao, X. P.; Pan, D.; Wei, D. H.; Zhao, J. H. Large tunable perpendicular magnetic anisotropy in ultrathin Co-based ferromagnetic films induced by antiferromagnetic δ-Mn. *Phys. Rev. Appl.* **2023**, *19*, No. 024033.

(10) Xiang, G.; Holleitner, A. W.; Sheu, B. L.; Mendoza, F. M.; Maksimov, O.; Stone, M. B.; Schiffer, P.; Awschalom, D. D.; Samarth, N. Magnetoresistance anomalies in (Ga,Mn)As epilayers with perpendicular magnetic anisotropy. *Phys. Rev. B* **2005**, *71*, No. 241307.

(11) Desrat, W.; Kamara, S.; Terki, F.; Charar, S.; Sadowski, J.; Maude, D. K. Antisymmetric magnetoresistance anomalies andmagnetic domain structure in GaMnAs/InGaAs layers. *Semicond. Sci. Technol.* **2009**, *24*, No. 065011.

(12) Niu, W.; Cao, Z.; Wang, Y. L.; Wu, Z. Q.; Zhang, X. Q.; Han, W. B.; Wei, L. J.; Wang, L. X.; Xu, Y. B.; Zou, Y. M.; He, L.; Pu, Y. Antisymmetric magnetoresistance in Fe_3GaTe_2 nanodevices of inhomogeneous thickness. *Phys. Rev. B* **2021**, *104*, No. 125429.

(13) Liu, P.; Liu, C. X.; Wang, Z.; Huang, M.; Hu, G. J.; Xiang, J. X.; Feng, C.; Chen, C.; Ma, Z. W.; Cui, X. D.; Zeng, H. L.; Sheng, Z. G.; Lu, Y. L.; Yin, G.; Chen, G.; Liu, K.; Xiang, B. Planar-symmetry-breaking induced antisymmetric magnetoresistance in van der Waals ferromagnet Fe_3GaTe_2. *Nano Res.* **2022**, *15*, 2531−2536.

(14) Miao, W. T.; Zhen, W. L.; Tan, C.; Wang, J.; Nie, Y.; Wang, H. N.; Wang, L.; Niu, Q.; Tian, M. L. Nonreciprocal antisymmetric magnetoresistance and unconventional hall effect in a two-dimensional ferromagnet. *ACS Nano* **2023**, *17*, 25449−25458.

(15) Hu, G. J.; Guo, H.; Lv, S. H.; Li, L. X.; Wang, Y. H.; Han, Y. C.; Pan, L. L.; Xie, Y. L.; Yu, W. Q.; Zhu, K.; Qi, Q.; Xian, G. Y.; Zhu, S. Y.; Shi, J. N.; Bao, L. H.; Lin, X.; Zhou, W.; Yang, H. T.; Gao, H.-J. Room-temperature antisymmetric magnetoresistance in van der Waals ferromagnet Fe_3GaTe_2 Nanosheets. *Adv. Mater.* **2024**, *36*, No. 2403154.

(16) Jiang, L. X.; Li, Q. C.; Li, J. F.; Guo, H. R.; Wu, C. W.; Luo, Z. J.; Xiong, R.; Zeng, M.; Luo, Z. C.; Zhao, J. K.; Chen, Z. X.; Zhang, Z. W.; Wu, H. Room-temperature spin-logic operations in van der Waals ferromagnet Fe_3GaTe_2. *Nano Lett.* **2025**, *25*, 9712−9718.

(17) Gao, X.; Wang, K. M.; Zhai, K.; Yan, J. X.; Yue, D. D.; Mu, C. P.; Yu, Z. P.; Cheng, Y. C.; Nie, A. M.; Liu, Z. Y. Modulation of magnetic domain and the occurrence of antisymmetric magnetoresistance in the folded van der Waals ferromagnet Fe_3GaTe_2. *Adv. Mater.* **2025**, *37*, No. 2420505.

(18) Hu, G. J.; Zhu, Y. M.; Xiang, J. X.; Yang, T.-Y.; Huang, M.; Wang, Z.; Wang, Z.; Liu, P.; Zhang, Y.; Feng, C.; Hou, D. Z.; Zhu, W. G.; Gu, M.; Hsu, C.-H.; Chuang, F.-C.; Lu, Y. L.; Xiang, B.; Chueh, Y.-L. Antisymmetric Magnetoresistance in a vander Waals antiferromagnetic/ferromagnetic layered $MnPS_3/Fe_3GeTe_2$ stacking heterostructure. *ACS Nano* **2020**, *14*, 12037−12044.

(19) Albarakati, S.; Tan, C.; Chen, Z.-J.; Partridge, J. G.; Zheng, G. L.; Farrar, L.; Mayes, E. L. H.; Field, M. R.; Lee, C.; Wang, Y. H.;

Xiong, Y. M.; Tian, M. L.; Xiang, F. X.; Hamilton, A. R.; Tretiakov, O. A.; Culcer, D.; Zhao, Y.-J.; Wang, L. Antisymmetric magnetoresistance in van der Waals Fe_3GeTe_2/graphite/Fe_3GeTe_2 trilayer heterostructures. *Sci. Adv.* **2019**, *5*, No. eaaw0409.
(20) Wu, Q. M.; Cui, Z. Z.; Zhu, M.; Jiang, Z. Y.; Fu, Z. P.; Lu, Y. L. Exchange bias controlled antisymmetric-symmetric magnetoresistances in Fe_3GeTe_2/graphite/Fe_3GeTe_2 trilayer. *2D Mater.* **2023**, *10*, No. 025009.
(21) Huang, B.; Clark, G.; Navarro-Moratalla, E.; Klein, D. R.; Cheng, R.; Seyler, K. L.; Zhong, D.; Schmidgall, E.; McGuire, M. A.; Cobden, D. H.; Yao, W.; Xiao, D.; Jarillo-Herrero, P.; Xu, X. D. Layer-dependent ferromagnetism in a van der Waals crystal down to the monolayer limit. *Nature* **2017**, *546*, 270−275.
(22) Gu, E.; Hope, S.; Tselepi, M.; Bland, J. A. C. Two-dimensional paramagnetic-ferromagnetic phase transition and magnetic anisotropy in Co (110) epitaxial nanoparticle arrays. *Phys. Rev. B* **1999**, *60*, 4092−4095.
(23) Kodama, R. H.; Berkowitz, A. E. Atomic-scale magnetic modeling of oxide nanoparticles. *Phys. Rev. B* **1999**, *59*, 6321−6336.
(24) Roth, W. L. Magnetic structures of MnO, FeO, CoO, and NiO. *Phys. Rev.* **1958**, *110*, 1333−1341.
(25) Xi, H. W.; White, R. M. Antiferromagnetic thickness dependence of exchange biasing. *Phys. Rev. B* **2000**, *61*, 80−83.
(26) Wang, W. X.; Yang, Y.; Naganuma, H.; Ando, Y.; Yu, R. C.; Han, X. F. The perpendicular anisotropy of $Co_{40}Fe_{40}B_{20}$ sandwiched between Ta and MgO layers and its application in CoFeB/MgO/CoFeB tunnel junction. *Appl. Phys. Lett.* **2011**, *99*, No. 012502.
(27) Schumacher, F. On the modification of the Kondorsky function. *J. Appl. Phys.* **1991**, *70*, 3184−3187.
(28) Liu, Q. B.; Liu, L.; Xing, G. Z.; Zhu, L. J. Asymmetric magnetization switching and programmable complete Boolean logic enabled by long-range intralayer Dzyaloshinskii-Moriya interaction. *Nat. Commun.* **2024**, *15*, 2978.
(29) In our system, it would be more precise to distinguish between the "top interfacial Co" and the "bottom interfacial Co." However, to maintain consistency with the literature, we adhere to the established convention (interfacial versus bulk Co) used in ref 18..
(30) Wang, B.-Y.; Lin, P.-H.; Tsai, M.-S.; Shih, C.-W.; Lee, M.-J.; Huang, C.-W.; Jih, N.-Y.; Wei, D.-H. Antiferromagnet-induced perpendicular magnetic anisotropy in ferromagnetic/ antiferromagnetic/ferromagnetic trilayers. *Phys. Rev. B* **2016**, *94*, No. 064402.
(31) Feng, J. F.; Wei, H. X.; Ren, Y.; Li, X. X.; Han, X. F. Magnetoresistance enhancement in a perpendicular $(Co/Pt)_4$/Co/IrMn/$(Co/Pt)_2$/Co structure. *J. Appl. Phys.* **2022**, *132*, No. 064506.
(32) Yuasa, S.; Nagahama, T.; Suzuki, Y. Spin-polarized resonant tunneling in magnetic tunnel junctions. *Science* **2002**, *297*, 234−237.
(33) Nozaki, T.; Jiang, Y.; Kaneko, Y.; Hirohata, A.; Tezuka, N.; Sugimoto, S.; Inomata, K. Spin-dependent quantum oscillations in magnetic tunnel junctions with Ru quantum wells. *Phys. Rev. B* **2004**, *70*, No. 172401.
(34) Tsymbal, E. Y.; Sokolov, A.; Sabirianov, I. F.; Doudin, B. Resonant inversion of tunneling magnetoresistance. *Phys. Rev. Lett.* **2003**, *90*, No. 186602.
(35) Mukhopadhyay, S.; Das, I. Inversion of magnetoresistance in magnetic tunnel junctions: effect of pinhole nanocontacts. *Phys. Rev. Lett.* **2006**, *96*, No. 026601.
(36) Bapna, M.; Parks, B.; Oberdick, S. D.; Almasi, H.; Wang, W. G.; Majetich, S. A. Spin-orbit-torque switching in 20-nm perpendicular magnetic tunnel junctions. *Phys. Rev. Appl.* **2018**, *10*, No. 024013.
(37) Chen, X. Z.; Higo, T.; Tanaka, K.; Nomoto, T.; Tsai, H.; Idzuchi, H.; Shiga, M.; Sakamoto, S.; Ando, R.; Kosaki, H.; Matsuo, T.; Nishio-Hamane, D.; Arita, R.; Miwa, S.; Nakatsuji, S. Octupole-driven magnetoresistance in an antiferromagnetic tunnel junction. *Nature* **2023**, *613*, 490−495.
(38) Fan, X. Y.; Zhu, H. F.; Mi, J. J.; Li, L. J. Antisymmetric tunneling magnetoresistance in Van der Waals Fe_3GeTe_2/Nb_3Cl_8/Fe_3GeTe_2 heterostructures driven by spin-splitting potential barrier. *Adv. Funct. Mater.* **2026**, *36*, No. e11716.
(39) Kao, I.-H.; Tang, J.; Ortiz, G. C.; Zhu, M.; Yuan, S.; Rao, R.; Li, J.; Edgar, J. H.; Yan, J.; Mandrus, D. G.; Watanabe, K.; Taniguchi, T.; Hwang, J.; Cheng, R.; Katoch, J.; Singh, S. Unconventional unidirectional magnetoresistance in heterostructures of a topological semimetal and a ferromagnet. *Nat. Mater.* **2025**, *24*, 1049−1057.
(40) Jiang, B. Y.; Wang, L. Y.; Bi, R.; Fan, J. W.; Zhao, J. J.; Yu, D. P.; Li, Z. L.; Wu, X. S. Chirality-dependent Hall effect and antisymmetric magnetoresistance in a magnetic Weyl semimetal. *Phys. Rev. Lett.* **2021**, *126*, No. 236601.
(41) Wang, Z.; Xiang, Y.; Chen, R.; Sun, Z.; Hong, C.; Chen, X.; Gao, J.; Wu, S.; Guo, Z.; Chen, Y.; Mi, Q.; Liu, Z.; Yan, S.; Lei, H.; Ruan, W.; Zhang, Y.; Yu, W.; Liu, W.-T.; Yuan, Z.; Wu, S. Ferromagnet-like binary switching of a Stoner−Wohlfarth antiferromagnet. *Nature* **2026**, *650*, 340−345.
(42) Feng, J. F.; Chen, P.; Liu, S. Q.; Wei, H. X.; Guo, J. H.; Wang, G. Y.; Huang, H.; Zhang, M.; Lu, M.; Han, X. F. Quantum well oscillations in giant magnetoresistance and conductance with ferromagnetic free layer thickness in spin-valve structures with inverted $[Co/Pt]_n$/Co reference layer. *J. Mag, Mag. Mater.* **2024**, *601*, No. 172177.

https://doi.org/10.1021/acs.nanolett.6c00125
Nano Lett. 2026, 26, 3258−3265